Research Square

Preprints are preliminary reports that have not undergone peer review.
They should not be considered conclusive, used to inform clinical practice,
or referenced by the media as validated information.

Development of a Wire-Renewal EDM Milling Electrode for Fabricating Microlens Array Molds with High Shape Accuracy on Tungsten Carbide

Md Nasir Uddin
Fubin Ma
Tianfeng Zhou
Liheng Gao
Gang Wang
Weijia Guo

guo_weijia@bit.edu.cn

Beijing Institute of Technology

Research Article

Keywords: Electrical discharge machining, Wire-renewal EDM milling, Tungsten carbide, Microlens array.

Posted Date: July 6th, 2026

DOI: https://doi.org/10.21203/rs.3.rs-9831146/v1

License: This work is licensed under a Creative Commons Attribution 4.0 International License.
Read Full License

Development of a Wire-Renewal EDM Milling Electrode for Fabricating Microlens Array Molds with High Shape Accuracy on Tungsten Carbide

Md Nasir Uddin [a], Fubin Ma [a, c, d], Tianfeng Zhou [a, b], Liheng Gao [a], Gang Wang [a], Weijia Guo [a, *]

a Department of Mechanical Engineering, Beijing Institute of Technology, Beijing 100081, China
b Beijing Institute of Technology, Chongqing Innovation Center, Chongqing 401120, China
c Beijing Institute of Precision Mechatronics and Controls, Beijing, 100076, China
d Innovation Center of Control Actuators, Beijing, 100076, China
Corresponding author: guo_weijia@bit.edu.cn

Abstract

Electrical discharge machining (EDM) is an effective technique for fabricating structured-array surfaces on tungsten carbide (WC) molds, owing to their hardness and thermal stability. However, conventional EDM faces significant challenges, particularly due to electrode wear, which necessitates frequent replacement and compromises form accuracy, thus limiting the efficiency of microlens array (MLA) fabrication. In this study, a wire-renewal EDM milling electrode was proposed and developed to overcome these limitations. The electrode features a spherical head integrated with a precision-contoured groove that holds a continuously tensioned copper wire, enabling in situ wire renewal and stable annular discharge. The mechanism of rotationally averaged annular discharge and its influence on material removal were investigated, and a comprehensive electro-thermal model was developed to describe the process. Key parameters, including spindle rotation speed, pulse width, pulse interval, servo voltage, and peak current, were systematically optimized, demonstrating that rotation and pulse timing are critical in mitigating center-biased material removal, while voltage and current primarily affect removal rate and aperture size. Under optimized conditions, a (5×5) MLA mold was fabricated on WC with uniform depth, coplanarity, and low form error, confirming high-accuracy and reproducible microlens formation. The proposed wire-renewal EDM milling strategy provides a robust solution for scalable and precise micro-optics manufacturing.

Keywords

Electrical discharge machining; Wire-renewal EDM milling; Tungsten carbide; Microlens array.

1. Introduction

Microlens arrays (MLAs) are crucial micro-optical elements used in a wide range of applications such as imaging systems [1, 2], optical communications [3], LiDAR [4], light-field cameras [5, 6], and biomedical imaging [7, 8]. Due to their ability to control light propagation with high precision, MLAs are indispensable in modern technologies such as augmented and virtual reality [9], 3D sensing, and advanced microscopy [10, 11]. The demand for mass production of high-quality MLAs has made precision glass molding the most promising method, where the quality of the microlens mold is crucial for the fidelity, optical performance, and durability of the replicated MLAs [12, 13]. Tungsten carbide (WC), with its exceptional hardness, wear resistance, and thermal stability, is the material of choice for microlens molds [14] as it can endure high-

temperature glass molding cycles without significant dimensional degradation. However, machining WC into fine micro-optical structures with high accuracy remains a major challenge [15], as conventional ultra-precision machining techniques such as grinding, diamond turning, and micro-milling suffer from rapid tool wear and poor form accuracy [16–18]. Electrical Discharge Machining (EDM) has emerged as a viable solution for machining hard and brittle materials like WC. Unlike traditional machining, EDM removes material via electrical discharges rather than mechanical contact, making it particularly effective for difficult-to-machine materials [19, 20]. However, the electrode wear during the machining process poses a significant limitation, as the electrode head becomes worn and roughened after machining even a single microlens. This results in progressive deterioration of form accuracy, surface quality, and uniformity of subsequent cavities, which is especially problematic for dense MLA fabrication, where frequent electrode replacement or trimming is necessary. These interruptions not only increase machining time and costs, but also complicate the alignment and indexing of cavities during array fabrication.

To improve the surface quality and manufacturing efficiency of the machined workpiece, many researchers have proposed novel EDM methods to optimize the discharge process. Zhou et al. [21] fabricated a microlens cavity on WC and silicon carbide using tilted EDM. The workpiece's surface roughness was approximately 1 μm, which was reduced by around 60% when the tilt angle was set to 25°. This approach was aimed at improving both machining efficiency and surface quality for difficult-to-machine materials. Jangra et al. [22] designed a Taguchi experiment and applied the grey relational analysis method to evaluate the impact of wire electrical discharge machining (WEDM) parameters on WC material containing 5.3% cobalt (Co). Talla et al. [23] employed the response surface methodology to analyze the effects of various parameters during reverse EDM and identified the optimal processing conditions for mild steel materials using copper electrodes. Zhang et al. [24] introduced a magnetic field-assisted EDM method for machining Ti6Al4V, to enhance the machining characteristics of titanium superalloys. The experimental results demonstrated a significant reduction in both electrode wear rate and energy consumption when the magnetic field was applied. Wu et al. [25] developed rotary dentate disk foil electrodes for fabricating microstructures on stainless steel, successfully minimizing electrode wear during the process. Dong et al. [26] utilized a novel water-in-oil nanoemulsion dielectric for EDM, resulting in a lower relative electrode wear rate compared to conventional water-based dielectrics. Sable et al. [27] employed the response surface method to investigate the influence of WEDM discharge parameters on the machining quality of WC and developed a mathematical model for predicting performance. Jiang et al. [28] proposed a two-dimensional simulation model to predict the electrode wear geometry, thereby enhancing the accuracy of EDM by compensating for electrode wear. Wang [29] examined the re-sticking phenomenon during EDM machining of WC workpieces. The study focused on the effects of rotational speed, polarity, and discharge parameters on the machining of WC workpieces. Pei et al. [30] developed a mathematical model for fixed-length compensation to enhance machining accuracy. While reducing tool wear can improve accuracy to some extent, achieving the desired shape and precision often requires multiple electrode replacements and optimizations, particularly for complex parts. As a result, the design and optimization of electrodes are crucial for improving the effectiveness of the EDM process.

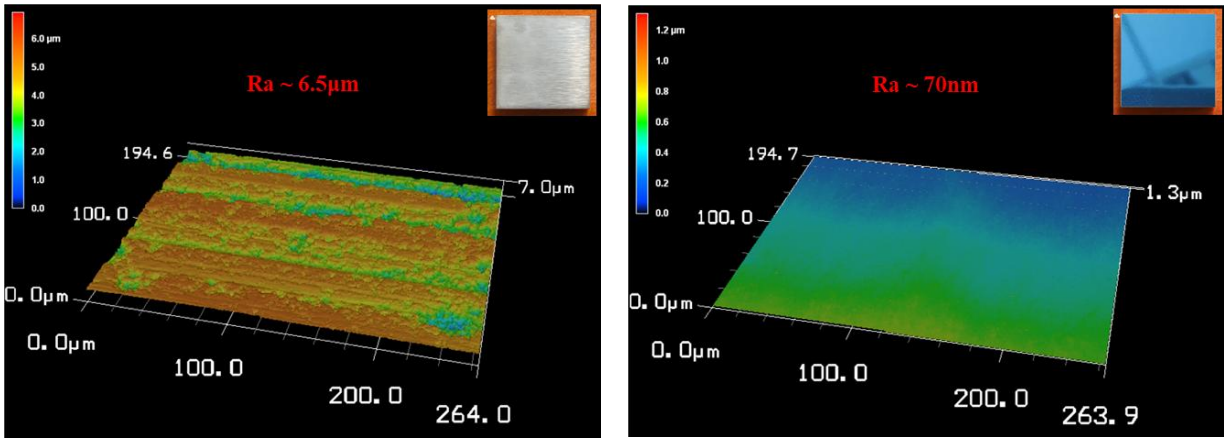
In recent years, an increasing number of researchers have focused on developing and studying various novel electrodes, with the goal of advancing the application of EDM in industrial settings. Takino and Hosaka [31] fabricated a 4×4 array on stainless steel using rod-shaped electrodes with spherical tips, demonstrating an innovative approach for array manufacturing. To fabricate 3D microstructures on 304 stainless steel, Xu et al. [32] proposed a micro-double-staged laminated object manufacturing method for preparing 3D micro-electrodes using wire EDM. To enhance machining efficiency in the EDM process, Gu et al. [33] proposed a bundled die-sinking electrode, designed to enable high-performance and cost-effective machining of Ti6Al4V alloys. To fabricate a square structure on 304 stainless steel while reducing electrode wear, Song et al. [34] proposed utilizing a strip electrode in the EDM process. Li et al. [35] introduced an innovative magnetic self-assembled ball electrode designed to simplify electrode replacement and boost processing efficiency in the fabrication of structured arrays. This method provides notable benefits compared to conventional integrated electrodes.

In conventional EDM, the preparation and replacement of electrodes are complex and time-consuming, directly affecting machining efficiency, accuracy, and reproducibility. These challenges limit the practical application of EDM for high-precision microstructures, such as microlens array (MLA) molds on hard materials like tungsten carbide. To overcome these limitations, this study proposes a novel wire-renewal EDM milling electrode, specifically designed to simplify electrode management while maintaining machining precision. The electrode features a rigid cylindrical shank that transitions into a spherical head with a precision-contoured groove, within which a copper wire is securely tensioned between upstream and downstream spools. During rotation, the wire conforms precisely to the spherical head, establishing a stable and controlled inter-electrode gap with the workpiece. This design enables in situ wire renewal, minimizing wear-induced variations and reducing the need for frequent electrode replacements. The electrode was fabricated and experimentally validated, demonstrating improved efficiency, consistent discharge stability, and high-accuracy microlens cavity formation.

2. Materials and Methods

2.1 Materials preparation

In this study, WC with two types of surface configuration was utilized for comparison. The square-shaped WC workpiece, comprising 94% WC powder and 6% Co powder, was supplied by Dayue Precision Metal Technology (Dongguan) Co., Ltd., with dimensions of 20 mm × 20 mm × 2 mm. The theoretical density is 14.9 g/cm³. The photograph and surface microscope image are shown in Fig. 1. The rough WC surface was cut from a long cuboid through wire EDM, with an average surface roughness of Ra ~ 6.5μm. It is taken as the first type of workpiece surface configuration and is characterized by uniformly distributed wire marks, as shown in Fig. 1(a). The polished surface was taken as the second type of surface configuration and was achieved through chemical-mechanical polishing (CMP) using silicon carbide abrasive paper with grit sizes of 400, 800, and 1000 in sequence. When switching to different grits of sandpaper, the polishing direction was changed by 90°, allowing the distinct shadowy traces left by the previous grit to be easily identified. Additionally, a diamond polishing agent was employed in the process. As a result, the polished surface showed an average roughness of Ra ~ 70 nm, as shown in Fig. 1(b).



(a) (b)

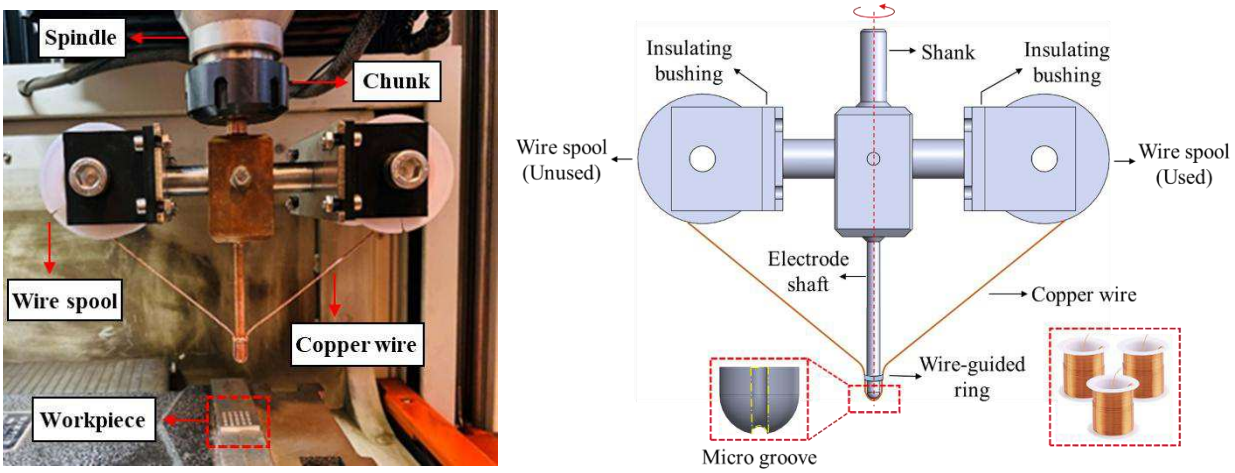
Figure. 1 The photograph and 3D surface microscope image: (a) wire EDM cut sample surface (Ra ~ 6.5μm); (b) polishing sample surface (Ra ~ 70nm).

2.2 Experimental details

2.2.1 Novel Electrode Design and MLA Fabrication Principle

This electrode features a rigid cylindrical shank that transitions into a spherical head integrated with a precision-machined, contoured groove. A copper wire is securely positioned within this groove and is tensioned between two spools, one located upstream and the other downstream. During rotation, the wire segment in the groove conforms to the spherical curvature of the head, thereby maintaining a stable and controlled inter-electrode gap with the workpiece.

As the electrode rotates, electrical discharges are initiated along the contoured wire, maintaining a consistent standoff distance and producing a rotationally averaged annular discharge region on the workpiece. Notably, the electrode's design allows for the in-situ renewal of the worn portion of the wire. This advancement ensures that the active discharge interface remains fresh without the need to reshape or replace the entire electrode. The dynamic renewal of the wire mitigates any wear-induced distortions, thereby stabilizing the discharge channel radius. This leads to the maintenance of a consistent, reproducible annular gap over prolonged machining cycles. The result is the self-averaging evolution of the cavities toward a spherical-cap morphology, while concurrently minimizing the growth of localized discharge hot-spots and preventing the imprinting of electrode shape onto the workpiece surface.



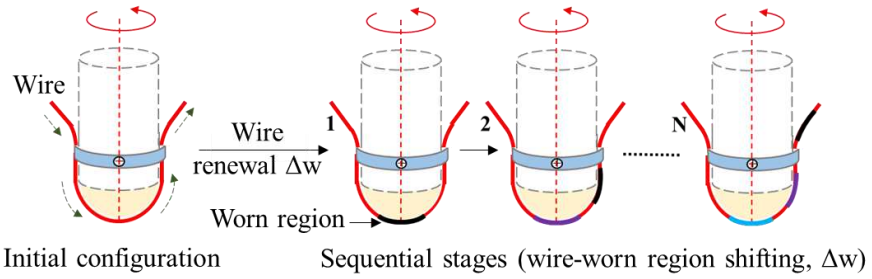
(a) (b)

Figure. 2 Wire-renewal EDM milling electrode design: (a) photograph of the designed electrode assembly mounted on the spindle; (b) schematic diagram of the integrated design.

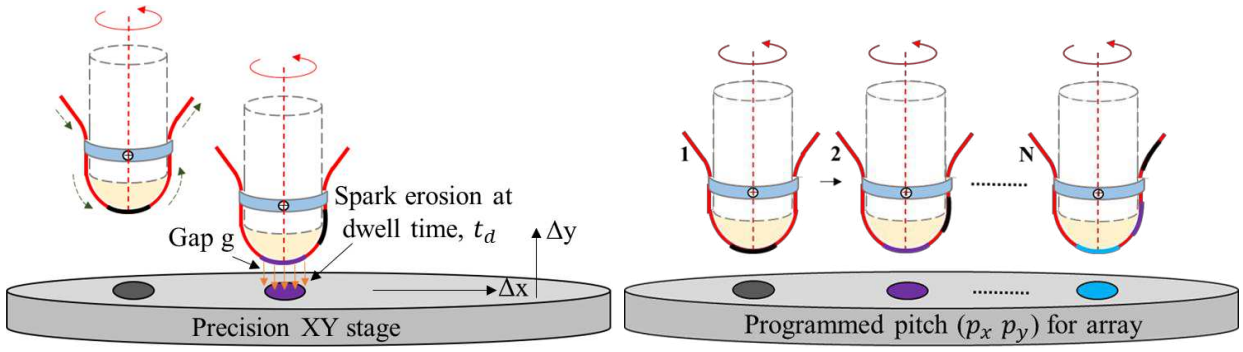
After each cavity is machined, the wire is indexed forward by a controlled increment Δw, advancing the spool to expose a fresh wire-surface segment. This dynamic renewal maintains a constant effective discharge radius and suppresses electrode-shape drift between successive lenslets. Assuming renewals occur at a fixed interval t and the total usable wire length is L_w, the nominal lenslet capacity is,

$$N_{max} = \frac{L_w}{\Delta w} \tag{1}$$

where N_{max} represents the maximum number of cavities that can be machined before wire replacement. Once a single cavity is machined to the desired depth, the electrode retracts and the precision XY stage shifts the workpiece by a programmed pitch (p_x, p_y). The spacing between adjacent cavities is determined by the pitch equation $p_x = D + s_x$ and $p_y = D + s_y$, where D is the lenslet diameter and s_x, s_y represent the inter-lens spacing.



(a)

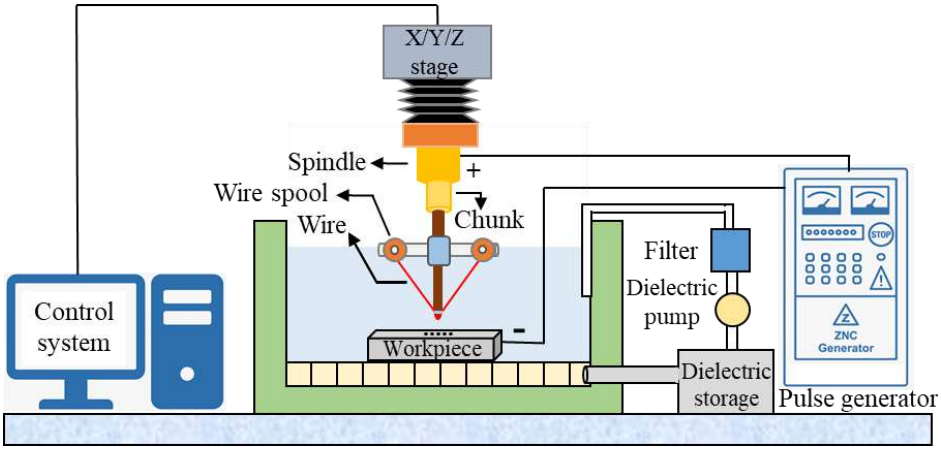


(b) (c)

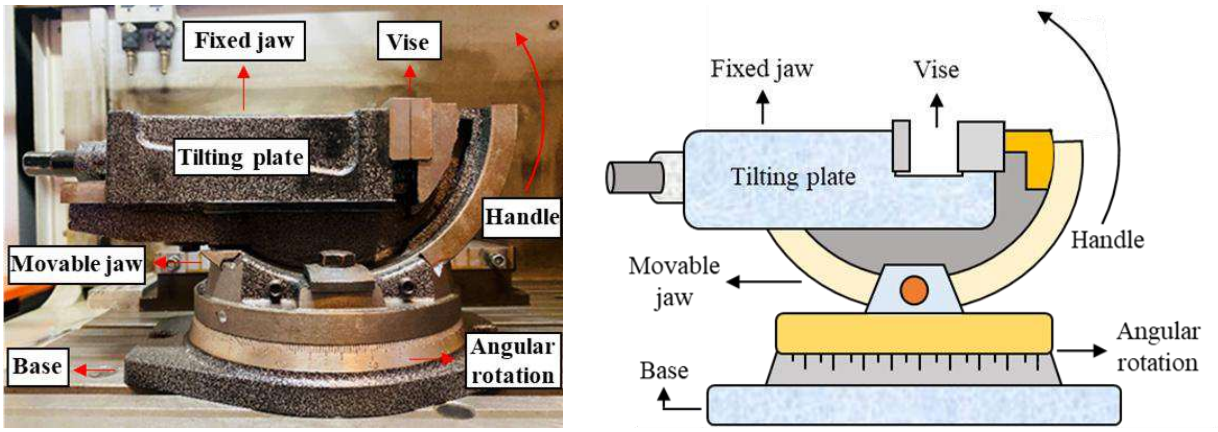
Figure. 3 Continuous MLAs fabrication process: (a) wire renewal by axial shift; (b) discharge and lenslet formation; (c) sequential lenslet array fabrication.

2.2.2 EDM Experimental Setup

The experiments were conducted on a CHARMILL ROBOFORM die-sinking EDM platform (Fig. 4a). The electrode was mounted on the Z spindle by the fixture; a copper wire was routed from an electrically insulated pay-off spool, seated within the precision-contoured groove of the electrode head, and collected on an insulated take-up spool. The electrical connection was established through the spherical head of the electrode, ensuring that discharges were confined to the contoured wire segment near the working gap. Accurate normal alignment between the electrode head and the workpiece was achieved using a compact tilting jig mounted beneath the workpiece (Fig. 4b-c).



(a)



(b) (c)

Figure. 4 EDM Experimental setup: (a) schematic of wire-renewal EDM milling; (b) photograph of the jig platform; (c) schematic diagram of the jig.

Table. 1: The machining condition of EDM

Types	Numbers or condition
Electrode	Electrode shaft (diameter = 5mm) Copper wire (diameter = 1mm) Groove (width = 1mm, depth = 0.50mm)
Workpiece material	Tungsten carbide (20 mm × 20 mm × 2 mm)
Working fluid	EDM-specific kerosene
Electrode polarity	Positive
Rotational speed (rpm)	20, 40, 60, 80, 100
Servo voltage (V)	80, 120, 160, 200
Peak current (A)	1, 1.5, 2, 3
Pulse width (μs)	3.2, 6.4, 25, 50
Pulse interval (μs)	3.2, 6.4, 25, 50

Table. 2: Machine default parameter setting

Group (E)	Servo voltage (V)	Peak current (A)	Pulse width (μs)	Pulse interval (μs)
202	200	1.5	25	25

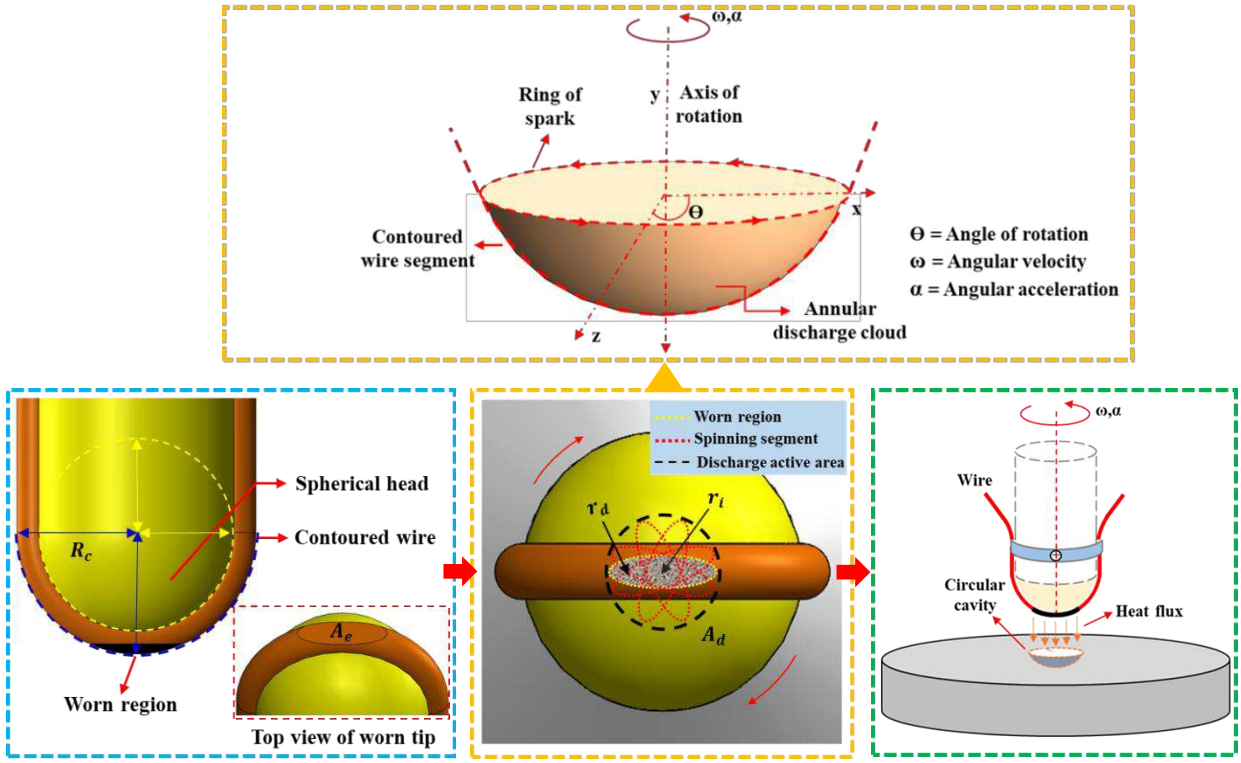
2.2.3 Characterization and measurements

The wear characteristics of the wire-renewal EDM milling electrode and the surface morphology of the fabricated lenslets were examined using a laser confocal microscope (VK-X100; Keyence, Osaka, Japan). The surface roughness of the MLA mold was quantified with a LEXT 3D optical profilometer (Olympus, Tokyo, Japan). Scanning Electron Microscopy (SEM) was used to examine the morphology of the cavity surfaces at both central and peripheral regions, revealing uniform micro-crater structures and resolidified features. Energy Dispersive X-ray Spectroscopy

(EDS) was applied to determine elemental composition, confirming material integrity and any compositional changes induced during EDM.

3. Lenslet Formation Mechanism and Surface Evolution Theory

The formation of each lenslet cavity in the proposed wire-renewal EDM milling process is driven by a combination of electro-thermal effects and geometric principles (Fig. 5).



(a) (b) (c)

Figure. 5 Lenslet formation using the proposed electrode: (a) wire electrode and worn region geometry; (b) spark ring formation by following annular discharge distribution; (c) heat flux leading to the lenslet.

During machining, it establishes a local inter-electrode separation determined by the combined curvatures of the wire and the spherical head electrode. This geometry concentrates the discharges within a small, elliptical closest-approach region on the wire. Over time, this region develops into a stable worn patch that reflects the iso-gap contour, which is progressively smoothed through use. As the electrode rotates, the worn patch is swept azimuthally, and its footprint overlaps across successive revolutions, creating an annular active discharge region on the workpiece, delimited by an inner ignition radius r_i and an outer active radius r_d.

3.1 Worn Zone Initiation and Elliptical Discharge Geometry

At the initiation of each EDM pulse, a transient plasma column forms between the copper wire (anode) and the tungsten carbide workpiece (cathode), bridging the inter-electrode gap. The mean current density J in this plasma column can be approximated by:

$$J = \frac{I}{A_P} \tag{2}$$

where I is the discharge current and A_p the plasma cross-sectional area. Due to the precision groove in the spherical head electrode, the wire conforms to the spherical profile, creating a small but systematic variation in the gap between the wire and the workpiece, following the wire's spherical contour.

Under a local quadratic (small-gap) approximation of the opposing surfaces that define the approach geometry, the normal separation about the point of closest approach, expressed in a wire-fixed frame (u, v) (with u along the wire axis and v circumferentially), is

$$s(u,v) \approx g_0 + \frac{1}{2}\left(k_{e,u} + k_{w,u}\right)u^2 + \frac{1}{2}\left(k_{e,v} + k_{w,v}\right)v^2 \tag{3}$$

where g_0 is the nominal interelectrode gap, $k_{e,u} = k_{e,v} = 1 / R_e$ for the spherical head electrode of radius R_e, and $k_{w,u} = 0$, $k_{w,v} = 1 / R_w$ for the wire of radius R_w. If material removal is activated wherever $s(u,v) \leq g_0 + \delta$ s (with $\delta > 0$ representing the effective discharge reach beyond the nominal gap), the worn region on the wire is an ellipse (Fig. 6).

$$\frac{u^2}{a^2} + \frac{v^2}{b^2} = 1 \tag{4}$$

with semi-axes

$$a = \sqrt{\frac{2\delta}{k_{e,u} + k_{w,u}}} = \sqrt{2\delta R_e} \tag{5}$$

$$b = \sqrt{\frac{2\delta}{k_{e,v} + k_{w,v}}} = \sqrt{\frac{2\delta}{\frac{1}{R_e} + \frac{1}{R_w}}} = \sqrt{\frac{2\delta R_e R_w}{R_e + R_w}} \tag{6}$$

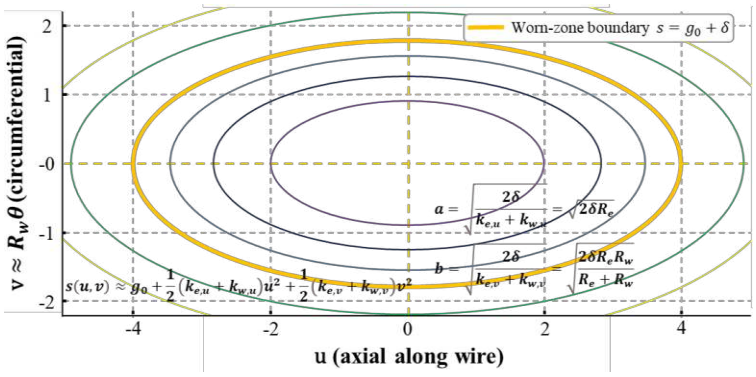


Figure. 6 Worn zone at the wire tip and the resulting elliptical discharge geometry.

Equivalently, in angular coordinates $v \approx R_w\theta$ on the wire surface, (4) becomes $u^2 / a^2 + (R_w\theta)^2 / b^2 \leq 1$. The corresponding instantaneous discharge region is:

$$A_e = \pi ab \tag{7}$$

Operationally, this elliptical worn region delineates the instantaneous spark-contact region- i.e., the locus of maximum erosion intensity at a given time step.

3.2 Rotational Transformation into a Circular Discharge Region

During the EDM process, the electrode rotates continuously around its central axis at an angular velocity $\omega(rad \cdot s^{-1})$. As the spindle rotates, the previously formed elliptical worn region on the wire is swept through multiple angular orientations. Each rotation leads to the superposition of discharge patterns from successive revolutions, generating a rotationally symmetric discharge region.

The effective discharge area over one full rotation can be obtained by angular averaging of the instantaneous discharge region. At each angular position, the discharge area is elliptical, and the total effective discharge area A_d for one full rotation is:

$$A_d = \frac{1}{2\pi}\int_0^{2\pi} A_e(\theta)\, d\theta \tag{8}$$

where, $A_e(\theta)$ is the discharge area at each angular position θ of the electrode. This angular integration captures the full sweep of the electrode's movement, and the result is the total effective discharge area.

As a result, the effective discharge region becomes a circular annulus, characterized by two distinct radii: inner radius r_i, where stable discharges initiate in each revolution and at the outer radius r_d, beyond which the plasma field decays below the ignition threshold. The total active discharge region can thus be described by the following expression:

$$A_d = \pi(r_d^2 - r_i^2) \tag{9}$$

Where r_i is the inner radius, determined by the minor semi-axis of the original elliptical discharge region, r_d is the outer radius, calculated as the root-sum-square of the semi-major and semi-minor axes of the ellipse:

$$r_d = \sqrt{a^2 + b^2} \tag{10}$$

Here, a and b are the semi-major and semi-minor axes of the ellipse formed during each rotation. These radii are then used to calculate the total active discharge area over the full revolution, ensuring uniform material removal.

3.3 Formation of the Rotational Heat Flux Field

Each spark discharge in the EDM process delivers a finite amount of thermal energy to the workpiece surface. Due to the spatial distribution of the plasma channel, this energy can be approximated as a Gaussian heat flux distribution at the point of discharge

$$q(r) = q_{max} exp\left(-\frac{r^2}{r_p^2}\right) \tag{11}$$

where q_{max} is the maximum heat flux at the discharge center, r is the radial distance from the discharge center, and r_p is the effective plasma radius.

As established previously, the rotation of the electrode transforms the instantaneous elliptical discharge into a circular annular discharge region. Consequently, the local heat flux is not applied at a single point but is distributed azimuthally over the annular region defined by inner radius r_i and outer radius r_d. Over multiple pulses and rotations, this leads to a rotationally averaged heat flux field. The cumulative heat input at a radial position r can therefore be expressed as a superposition of successive discharge events:

$$q_{eff}(r) = \frac{1}{2\pi}\int_0^{2\pi} q(r,\theta)\, d\theta \tag{12}$$

which results in a radially symmetric heat flux distribution concentrated within the annular discharge zone $r_i \le r \le r_d$, with peak intensity near the inner radius.

To evaluate the resulting temperature field, the workpiece is modeled as a semi-infinite solid subjected to a transient surface heat flux. The surface temperature rises at radial position r and time t is given by the classical heat conduction solution:

$$T(r,t) = \frac{1}{\rho c}\int_0^t \frac{q_{eff}(r,\tau)}{\sqrt{\pi\alpha(t-\tau)}}\, d\tau \tag{13}$$

where ρ, c, and k are the density, specific heat, and thermal conductivity of the workpiece material, respectively, and $\alpha = \frac{k}{\rho c}$ is the thermal diffusivity. For a single discharge pulse of duration t_{on}, assuming constant heat flux during the pulse, the peak surface temperature at the center of the discharge can be approximated as:

$$T_{max} \approx \frac{2q_m\sqrt{t_{on}}}{k\sqrt{\pi}} \tag{14}$$

This expression indicates that the temperature rise increases with both the heat flux intensity and the square root of the pulse duration, while being inversely proportional to the thermal conductivity of the material.

Material removal occurs when the local surface temperature exceeds the melting or vaporization threshold of tungsten carbide. Due to the rotational averaging effect, each radial position within the annular region experiences repeated thermal loading, resulting in a cumulative heat flux field. The inner region undergoes more frequent thermal cycling (higher duty exposure), leading to higher effective temperature and enhanced material removal compared to the outer region.

3.4 Development of Spherical-Cap Cavity

As a material removal process under this radially symmetric heat flux, the eroded surface gradually evolves toward a spherical-cap morphology. The material removal rate (MRR) during EDM

milling is proportional to the energy absorbed per discharge and inversely proportional to the discharge-active area. The incremental cavity depth after N sparks can be expressed as:

$$z(N) \approx \frac{\Delta V \cdot N}{A_d} \tag{15}$$

where, N is the mean erosion volume per spark and A_d is the effective discharge area. The shape evolution can be approximated by a geometric relation:

$$z(r) = R_c - \sqrt{R_c^2 - r^2} \tag{16}$$

where, R_c denotes the effective curvature radius of the lenslet. The curvature is determined by both the discharge area A_d and the volumetric removal rate V, which depend on the discharge energy per pulse E_P:

$$E_p = V_d . I_p . t_{on} \tag{17}$$

where, V_d is the discharge voltage, I_p is the peak discharge current, and t_{on} is the pulse duration. The MRR is proportional to the energy absorbed per spark, given by:

$$V \propto \eta \frac{E_P N}{A_d} \tag{18}$$

where η is the energy efficiency factor, and N is the number of pulses, and η. This equation highlights how the material removal rate is influenced by the discharge energy and the area of the spark.

4. Results and discussion

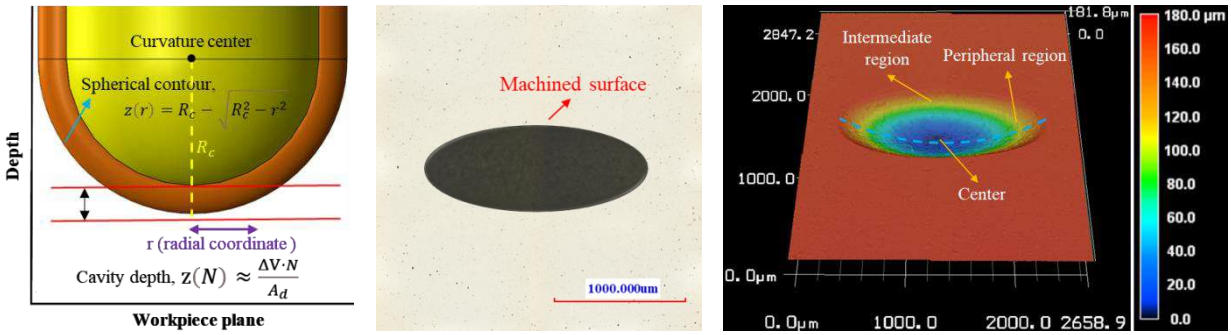
4.1 Cavity Shape Accuracy and Alignment

4.1.1 Static Material Removal

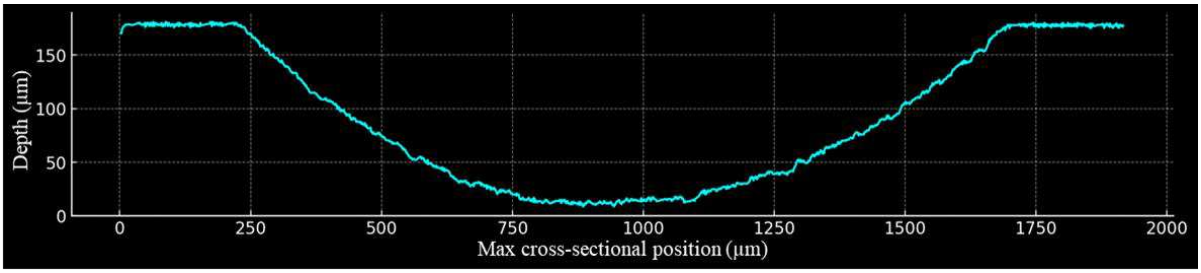
To verify that the contoured wire segment precisely conforms to the spherical electrode without introducing geometric distortion or flat regions at the discharge head, a static EDM test was performed. The electrode was held perpendicular to the workpiece, and machining was conducted without rotation, ensuring that the resulting machined profile accurately reflected the instantaneous geometry of the electrode.

The results, presented in Fig. 7, provide critical insight into the discharge behavior and electrode conformity. As shown in Fig. 7(a), the geometric model for the non-rotational discharge demonstrates that the opposing curvatures of the spherical head and seated wire create a small-gap quadratic configuration, predicting the formation of an elliptical high-incidence zone at the point of closest approach. The top-view of the optical microscopic image in Fig.7(b) shows an elliptical aperture, consistent with the planar projection of a spherical head. The confocal 3D topography in Fig. 7(c) further corroborated the model, revealing a smooth, radially graded depression with concentric iso-depth contours, indicative of axial symmetry and a continuous surface profile. The

cross-sectional profile (Fig. 7d) followed a circular-arc shape, demonstrating that the active wire segment conforms precisely to the spherical geometry of the electrode at the discharge interface.



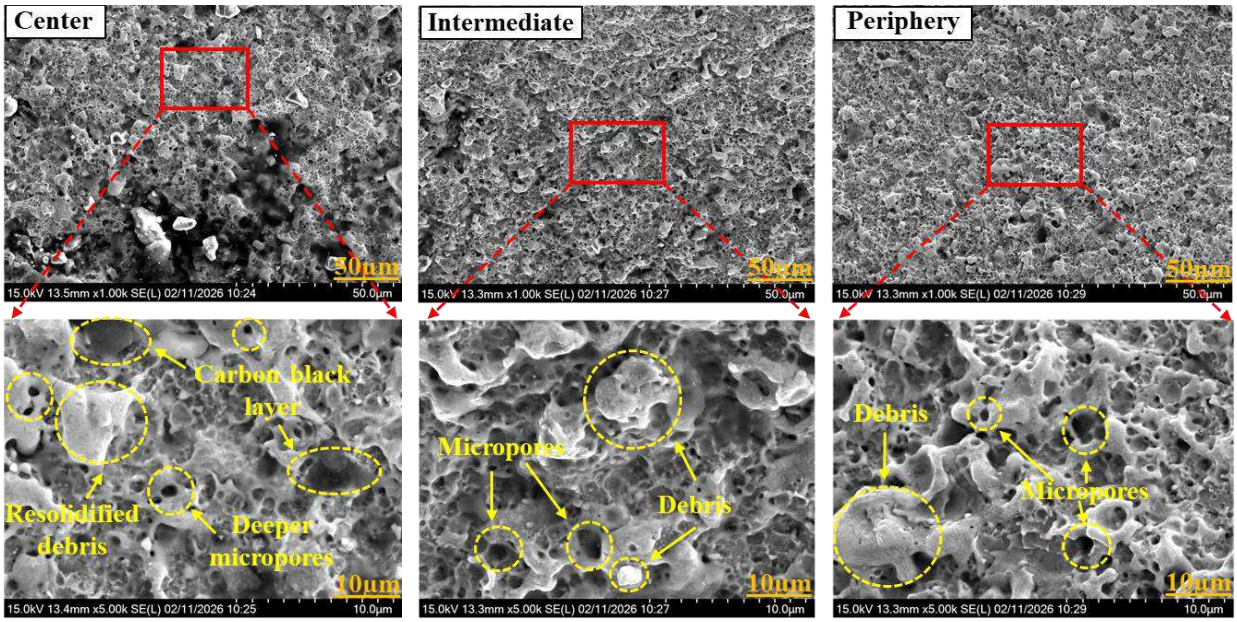
(a) (b) (c)



(c)

Figure. 7 Static material removal: (a) geometric model of EDM removal; (b) elliptical removal region on workpiece; (c) 3D topography with concentric grading; (d) cross-sectional profile.

To further assess surface morphology, SEM was used to examine three representative regions of the machined zone: the center, intermediate region, and peripheral regions. The SEM micrographs present characteristic thermo-electrical erosion features on the WC surface, including overlapping micropores, resolidified molten droplets, and microporosity. In the central region (Fig. 8a), larger and deeper micropores were observed, with agglomerated resolidified debris, indicating localized concentration of discharge energy and rapid melt-solidification cycles. The intermediate region (Fig. 8b) shows a more uniform distribution of micropores with reduced debris accumulation, suggesting more stable discharges and improved molten material expulsion. The peripheral region (Fig. 8c) shows finer craters and a more homogeneous surface texture, reflecting the gradual decay of discharge intensity toward the periphery. This positional gradient of erosion intensity across the static material removal zone substantiates that, under non-rotational conditions, the instantaneous discharge energy density is highest near the geometric center of the electrode and decreases radially outward.



(a) (b) (c)

Figure. 8 SEM analysis of static material removal: (a) at central region; (b) at intermediate region; (c) at peripheral region.

4.1.2 Restoration of Axial Symmetry

During the initial cavity formation using the wire-renewal EDM milling setup, an unintended deviation from axial symmetry was observed at a spindle speed of 20 rpm, with the process parameters held constant (Table 2). The 2D color height map in Fig. 9(a) represents an off-center depression, and the corresponding cross-sectional profile shown in Fig. 9(c) indicates that the minimum depth was displaced from the geometric center by approximately $\Delta x \approx 67$ µm. A linear baseline fit to the flank data yield a slope of m = -0.0089µm, which corresponds to an effective surface tilt of approximately -0.51° relative to the electrode's rotational plane.

To mitigate this geometric bias, the workpiece was mounted on a precision tilting jig, allowing fine angular adjustments in both the X and Y planes. Guided by the initial measurements, the workpiece was leveled to approximately 0.5°, ensuring it was parallel to the electrode's rotational plane. This adjustment resulted in a uniform discharge gap across the entire active region.

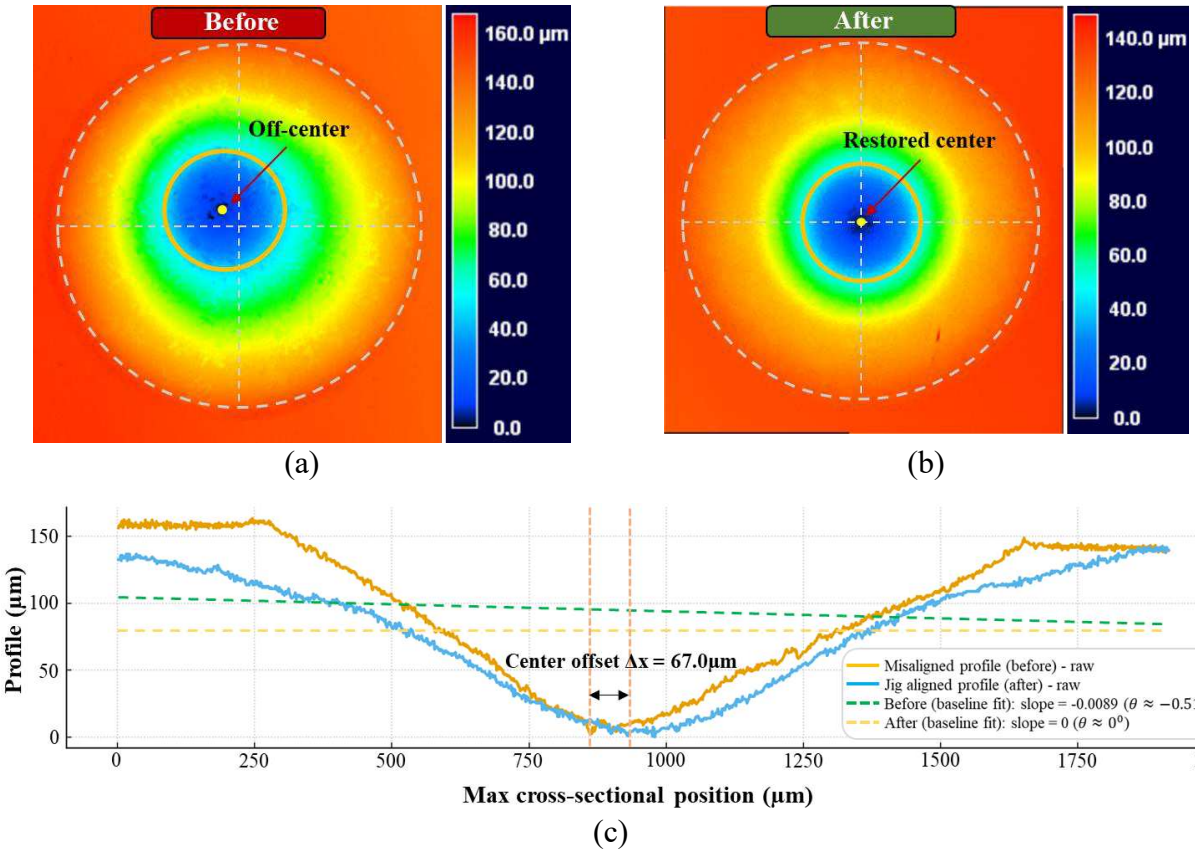


Figure. 9 Restoration of axial symmetry: (a) off-center before alignment; (b) restored center after jig alignment; (c) overlay of cross-sections before/after jig alignment.

Post-compensation results confirm the restoration of axial symmetry. The 2D color height map in Fig. 9(b) shows a concentric, centrally located cavity with a smooth radial gradient. The overlay of cross-sections in Fig. 9(c) shows that the depth minimum aligns with the geometric center after alignment, and the fitted baseline slope is effectively 0 ($\theta \approx 0^0$).

4.1.3 Center-Biased Material Removal from Rotational Discharge

During machining, a pronounced central material bias was observed despite the cavity opening's apparent circularity. As shown in Fig. 10(a), the top view of the surface appears circular, but the depth distribution is aspherical, characterized by a central dimple and roughened edge (Fig. 10b). The corresponding cross-sectional profile (Fig. 10d) indicates greater material removal at the cavity center, reflecting the concentration of discharge energy near the axis of rotation.

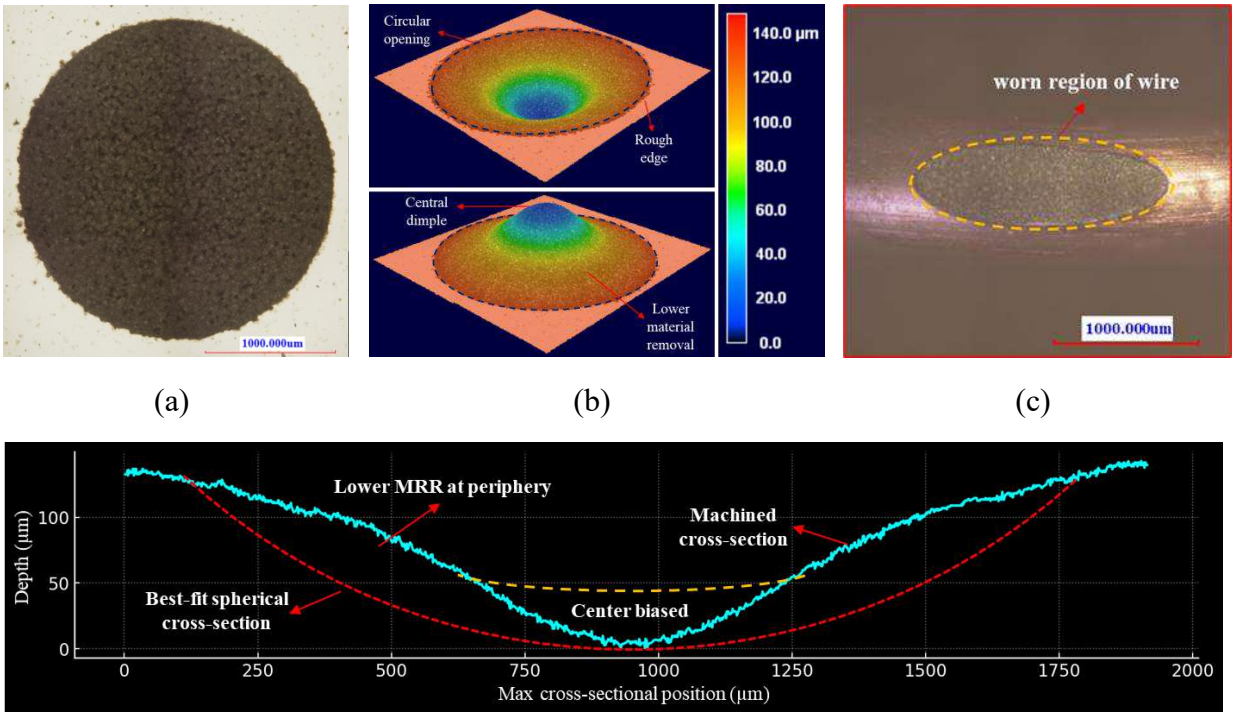


Figure. 10 Center-biased material removals: (a) circular opening surface of machined cavity; (b) 3D topography with aspheric depth; (c) elliptical worn region of wire electrode; (d) cross-section of the lenslet profile.

This behavior arises directly from the evolution of the discharge region and the associated rotationally averaged heat flux field. The local gap between the contoured wire and the workpiece can be approximated as a quadric surface, producing elliptical iso-gap contours (Fig. 11a). Upon machining each cavity, the closest-approach region on the wire develops into a localized elliptical discharge zone along the wire axis (Fig. 11a inset). As the spindle rotates, this discharge region is swept azimuthally, forming an annular active discharge zone, bounded by an inner radius (r_i) where stable discharges initiate and an outer radius (r_d) beyond which the plasma field falls below the ignition threshold (Fig. 11b). The resulting cumulative radial heat flux and the center-biased material removal pattern are illustrated in the top-view and cross-sectional cavity profile (Fig. 11c). This rotational transformation, shown in Fig. 11(b), results in a circularly symmetric active discharge region. The resulting cumulative radial heat flux can be approximated by a normalized Gaussian-type distribution:

$$Q(r) = \begin{cases} 1, & r \le r_i \\ exp\left(-\dfrac{r^2 - r_i^2}{r_d^2 - r_i^2}\right), & r_i < r \le r_d \\ 0, & r > r_d \end{cases} \tag{19}$$

Where, r is the radial distance from the center of the discharge. The rotationally averaged heat flux field, as described by Eq. (19), was implemented in Python using Matplotlib to generate the 2D color map shown in Fig. 11(d). This computational visualization simulates the radial energy

distribution across the annular discharge zone and provides a quantitative basis for analyzing center-biased material removal. This cumulative energy distribution leads to a peak material removal rate (MRR) at the cavity center, producing a deeper central profile relative to the periphery.

Two key kinematic effects underline this rotationally biased material removal: (i) a duty-cycle bias, where points near the inner radius are revisited more frequently during each revolution, enhancing thermal cycling and repeated melt-solidification; and (ii) the finite width of the discharge kernel, which delivers heat inward during each pass. These mechanisms accelerate material removal at the cavity center, producing the observed central material bias, even though the instantaneous discharge maintains an annular configuration.

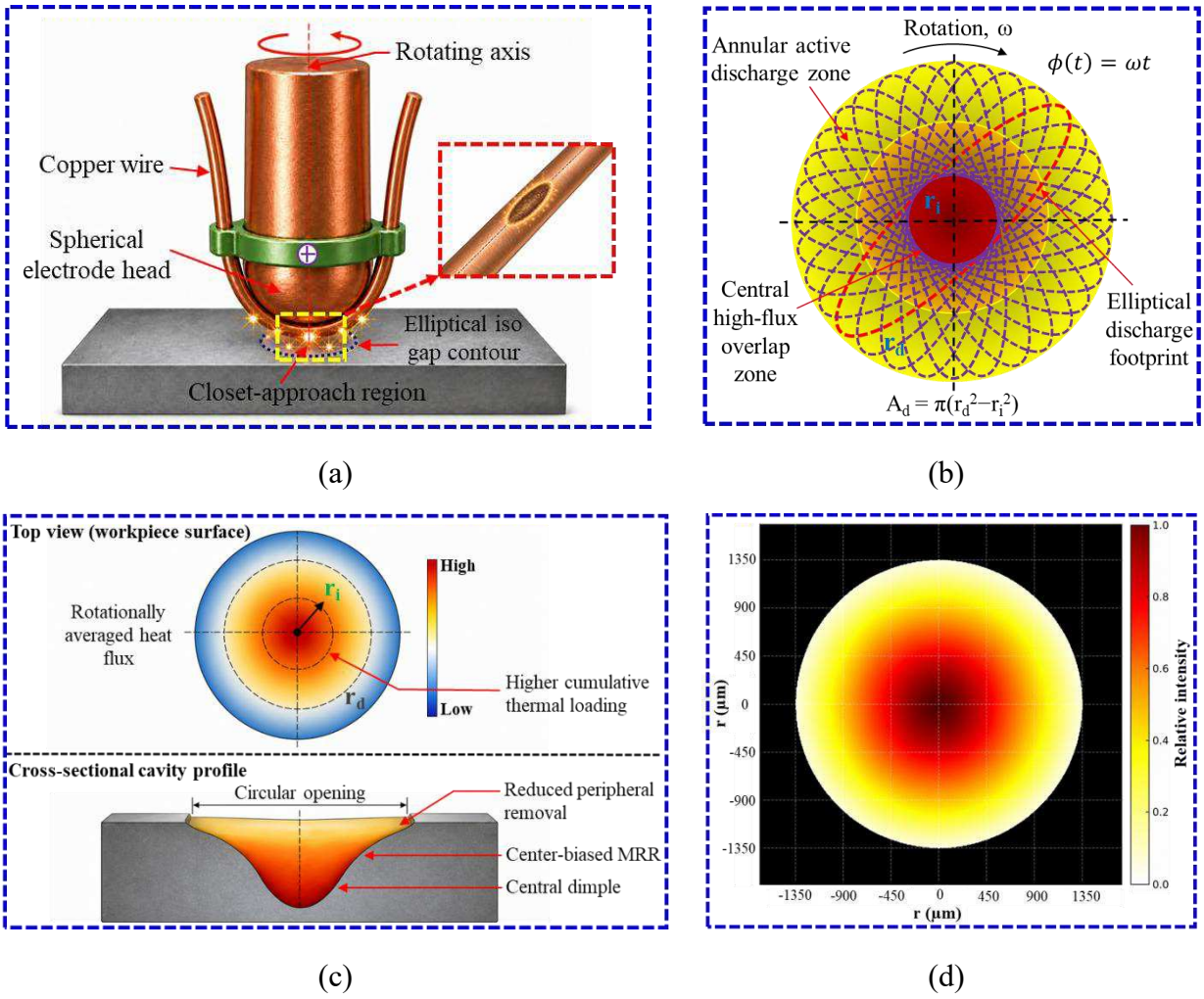
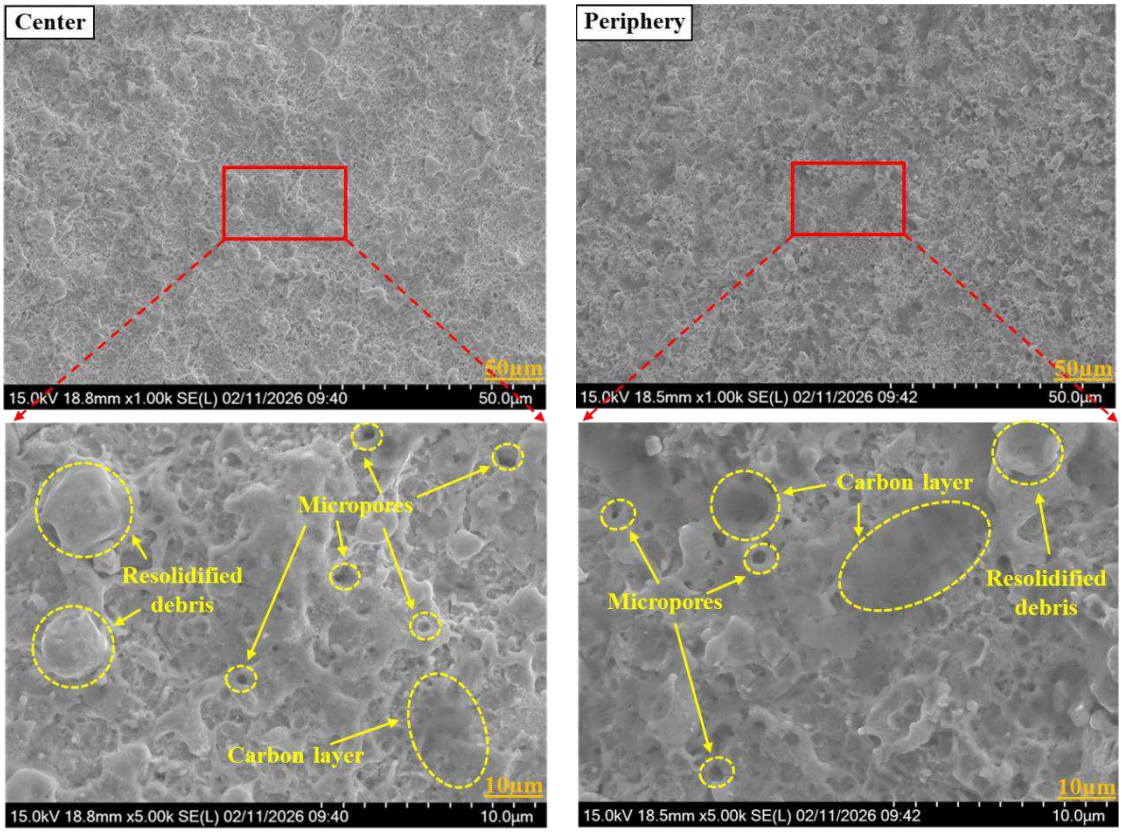


Figure. 11 Central material bias and annular discharge field: (a) local gap and elliptical iso-gap contours; (b) rotation forming annular zone; (c) heat flux and center biased cavity profile; (d) rotationally averaged heat flux map.

SEM analysis further supports this explanation. The central region (Fig. 12a) of the cavity shows densely overlapping micropores and resolidified molten features, indicative of repeated thermal

cycling and cumulative erosion. In contrast, the peripheral region (Fig. 12b) shows fewer, more isolated micropores, consistent with reduced energy deposition and slower material removal at larger radii. These observations confirm that the center-biased material removal is a direct consequence of the rotationally averaged discharge and associated radial heat flux distribution.



(a) (b)

Figure. 12 SEM characterization of cavity surface under rotational EDM conditions: (a) at central region; (b) at the peripheral region.

4.2 EDM Parametric Optimization and Cavity Characterization

The geometric and surface quality of the fabricated microlens cavities were evaluated using high-resolution 3D confocal microscopy. Key quantitative metrics-including the sag (maximum depth), width at half sag (WHS), root mean square (RMS) form error, and normalized RMS (NRMS)—were calculated to provide a comprehensive assessment of cavity geometry and fidelity.

The sag (maximum depth) is defined as the vertical distance between the geometric center of the cavity and its perimeter:

$$Sag = z_{center} - z_{edge} \tag{20}$$

Where, z_{center} is the height at the cavity center, and z_{edge} is the reference height at the cavity perimeter.

The half-sag height is calculated as:

$$z_{half} = z_{edge} + \frac{Sag}{2} \tag{21}$$

The width at half sag (WHS), representing the lateral aperture of the cavity at half of its maximum depth, is determined as:

$$WHS = r_2 - r_1 \tag{22}$$

where, r_1 and r_2 are the radial positions on opposite sides of the cavity corresponding to z_{half}.

The RMS form error quantifies the deviation of the measured cavity surface from the ideal spherical profile:

$$RMS = \sqrt{\frac{1}{N}\sum_{i=1}^{N}\left(z_i - z_{fit,i}\right)^2} \tag{23}$$

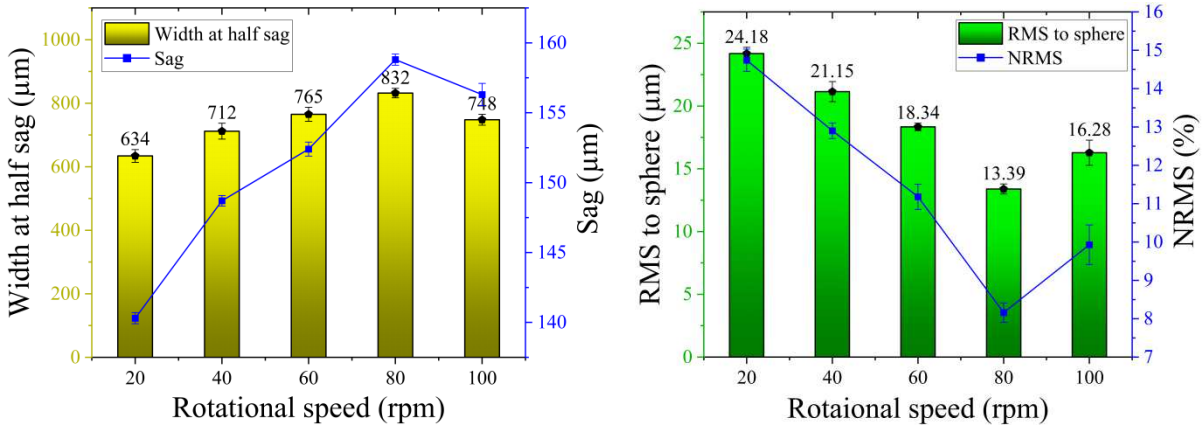
where z_i is the measured height at the point i, $z_{fit,i}$ is the corresponding height on the best-fit spherical surface, and N is the total number of measurement points.

The normalized RMS (NRMS) expresses the RMS deviation relative to the cavity sag, providing a dimensionless measure of surface form fidelity:

$$NRMS = \frac{RMS}{Sag} \times 100\% \tag{24}$$

4.2.1 Influence of Rotation and Pulse Timing

Spindle speed was varied from 20 to 100 rpm while all other process parameters were maintained as specified in Tab. 2. As shown in Fig. 13(a) and 13(b), a spindle speed of 80 rpm produced the most spherical lenslet profiles, with the WHS reaching a maximum of 832 µm. At this rotation rate, form error metrics were minimized, with RMS decreasing to 13.39 µm and NRMS to 8.16%. In contrast, lower spindle speeds (20-40 rpm) and higher speeds (100 rpm) resulted in suboptimal geometries, with larger form errors and reduced uniformity of the lenslet apertures.



(a) (b)

Figure. 13 Influence of rotational speed: (a) width at half sag and sag; (b) RMS to sphere and NRMS.

As shown in Fig. 14(a,b), the results indicate that a pulse width and interval of 25 μs yielded the most consistent cavity shapes. Under these conditions, WHS increased from 690 μm (3.2 μs) to 862.3 μm (50 μs), with the maximum sag observed at 163.4 μm. Pulse width shorter than 25 μs resulted in insufficient energy deposition, producing higher residual errors (RMS = 14.6-15.2 μm), whereas longer pulse width (50 μs) reduced the effective pulse frequency, weakening peripheral material removal and increasing RMS (19.13 μm) and NRMS (11.66%).

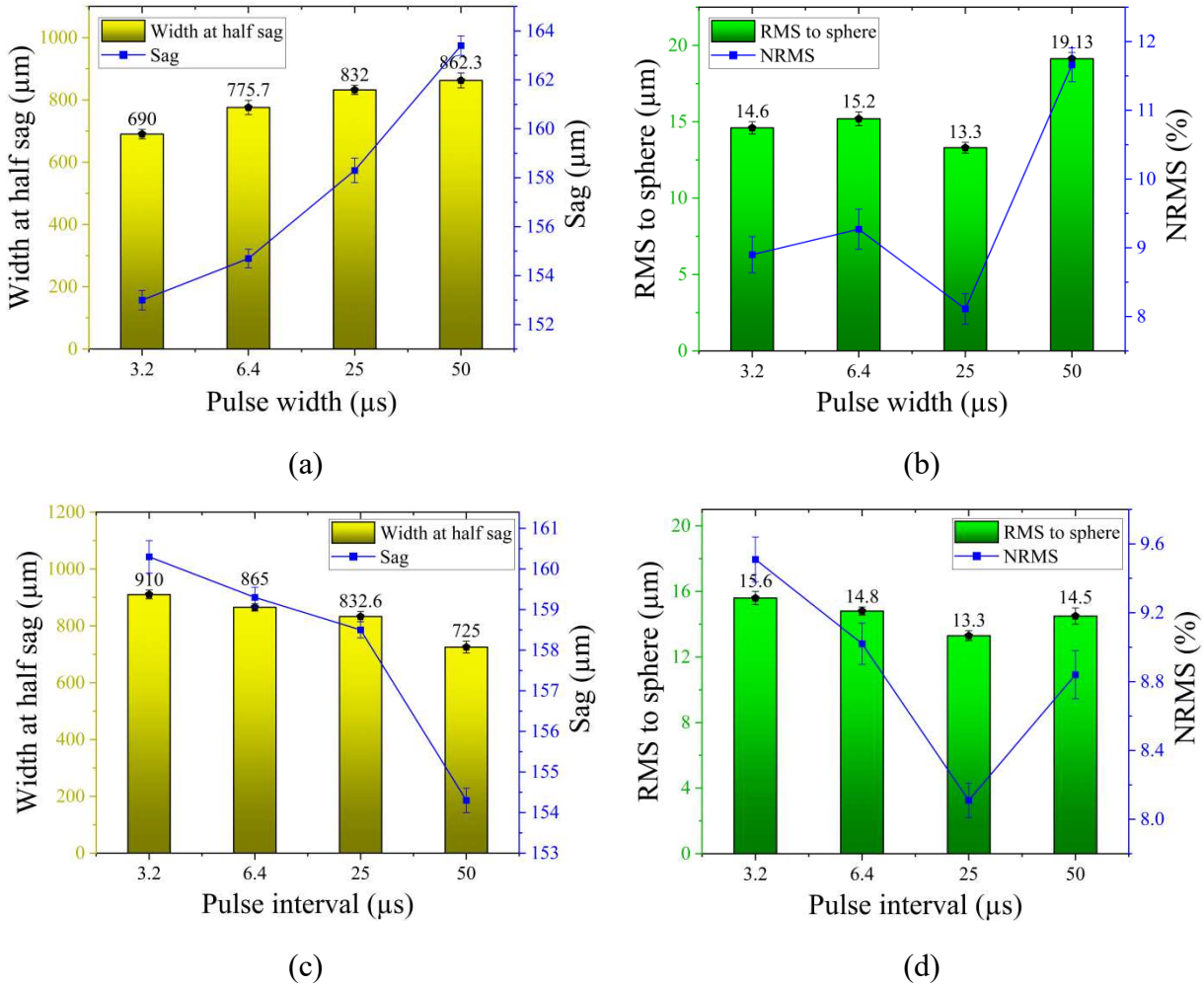


Figure. 14 Influence of pulse width and pulse interval: (a,c) width at half sag and sag; (b,d) RMS to sphere and NRMS.

As shown in Fig. 14(c,d), increasing the pulse interval resulted in a progressive decrease in the WHS, from 910 μm at 3.2 μs to 865 μm at 6.4 μs, 832.6 μm at 25 μs, and 725 μm at 50 μs. The corresponding cavity sag exhibited a slight reduction over the same interval range, decreasing from 160.3 μm to 159.3 μm, 158.5 μm, and 154.3 μm, with the minimum RMS and NRMS values observed at 25 μs (RMS = 13.3 μm; NRMS = 8.11%). Short pulse intervals (3.2-6.4 μs) were insufficient for complete deionization and effective debris removal, resulting in elevated RMS

values (14.8-15.6 μm). Conversely, excessively long pulse intervals (50 μs) reduced the effective pulse frequency, weakened peripheral material removal, and led to increased RMS (14.5 μm) and NRMS (8.84%).

4.2.2 Influence of Servo Voltage and Peak Current

Servo voltage was varied from 80 V to 200 V to investigate its influence on cavity dimensions and form accuracy (Fig. 15a,b). Increasing the servo voltage gradually reduced both the WHS and the sag depth, while simultaneously increasing the form error. Specifically, WHS decreased from 857.1 μm at 80 V to 832.5 μm at 200 V, accompanied by an increase in RMS from 3.9 μm to 13.1 μm. This trend is attributed to the role of servo voltage in controlling the nominal inter-electrode gap: higher voltages enlarge the working gap, reduce discharge utilization near the cavity periphery, and narrow the effective annular discharge zone, thereby diminishing spherical conformity. Within the tested range, a servo voltage of 80 V provides the widest aperture and the lowest form error and was therefore selected as the optimal setting.

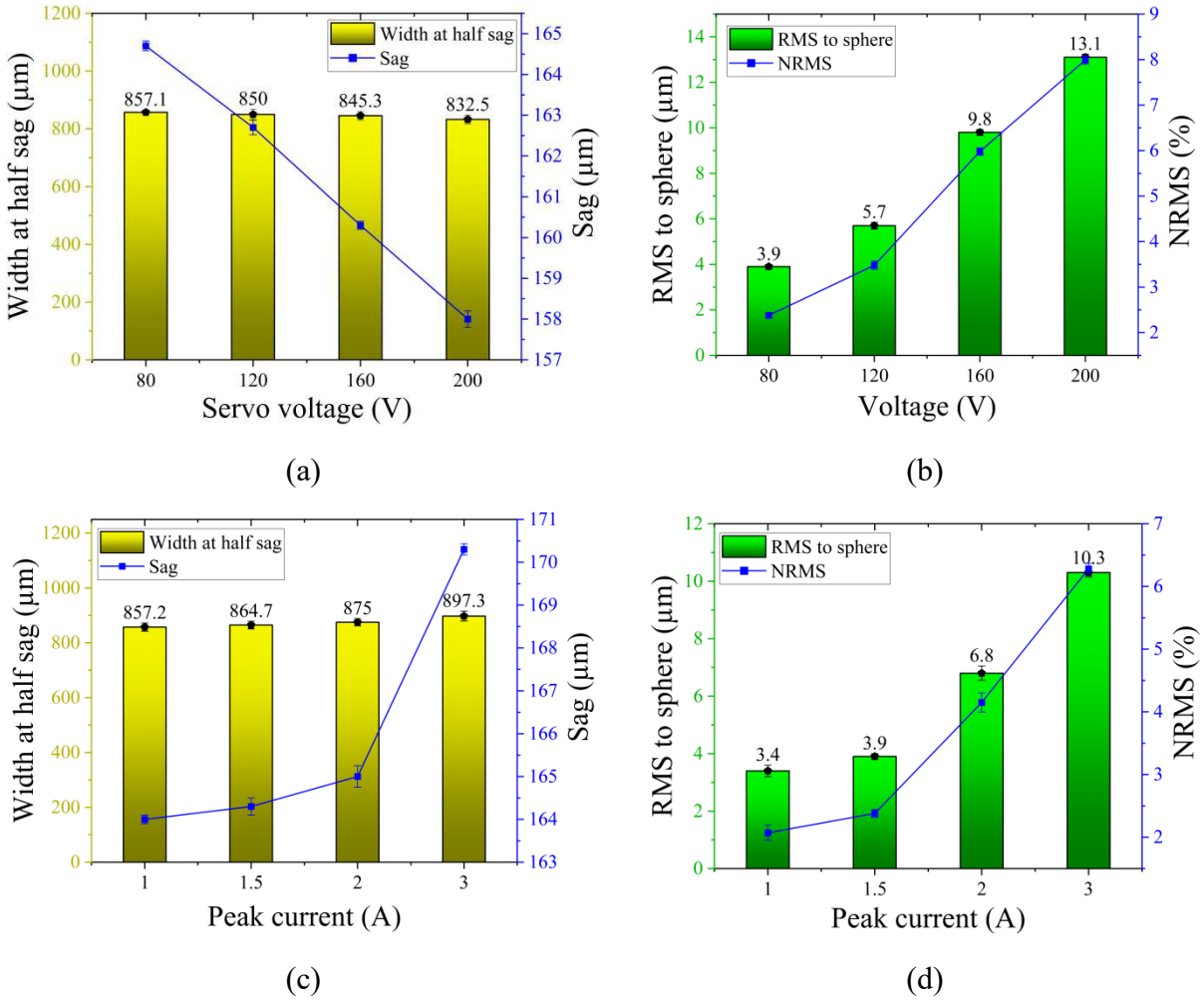


Figure. 15 Influence of servo voltage and peak current: (a,c) width at half sag and sag; (b,d) RMS to sphere and NRMS.

As shown in Fig. 15(c,d), increasing the peak current from 1 A to 3A enlarged the WHS and slightly increased the sag depth, indicating higher MRR due to increased discharge energy. However, excessive current degraded form fidelity. While RMS remained low at 1-1.5 A (3.4-3.9 μm), it increased significantly at higher currents, reaching 10.3 μm at 3A. This deterioration is associated with increased plasma pressure and unstable melt ejection, which induce irregular erosion and recast features. Consequently, a peak current of 1 A represents the optimal balance between aperture size and spherical accuracy for high-accuracy microlens fabrication.

The parametric study demonstrates that spindle rotation and pulse timing are the dominant factors in controlling center-biased material removal during EDM microlens fabrication. Proper selection of rotation speed ensures a uniform annular discharge, while optimized pulse width and interval provide consistent energy deposition, resulting in symmetric material removal across the cavity. In comparison, servo voltage and peak current primarily affect the overall material removal rate and aperture size conventionally. These results highlight that precise control of rotational kinematics and pulse parameters is essential for achieving high-accuracy, uniform microlens cavities, whereas voltage and current act as secondary tuning factors.

4.2.3 Analysis of Lenslet Morphology and Surface Composition

A representative microlens cavity was fabricated on a WC workpiece using EDM parameters optimized to minimize form error and ensure uniform cavity geometry. The optical top view (Fig. 16a) presents a circular aperture with smooth edges and no observable chipping. The confocal 3D surface mapping (Fig. 16b) shows a spherical-cap morphology with concentric iso-depth contours, indicating excellent axial symmetry and uniform material removal across the annular active region. Cross-sectional overlays (Fig. 16c) confirm near-perfect conformity to the best-fit spherical profile, showing no central dimple and enhanced peripheral material removal, resulting in flattened cavity shoulders.

The material removal volume (V), material removal rate (MRR), and surface roughness (S_a) were calculated following the method [14], which uses a point-cloud-based approach with the volume microelement method. According to this methodology, the material removal volume is determined by,

$$V = \sum_{p\in\Omega_2} \left(z_{plane}(x,y) - z_p\right) dxdy \tag{25}$$

The material removal rate is obtained as,

$$MRR = \frac{V}{T} \tag{26}$$

Where, T is the total machining time per cavity. The surface roughness is computed from the deviation of each measured point from the fitted spherical profile,

$$S_a = \frac{\Sigma_{p\in\Omega_2}\sqrt{(\|p-(x_0,y_0,z_0)\|-R)^2}}{\Sigma_{p\in\Omega_2}1} \tag{27}$$

where R is the fitted spherical radius, (x_0, y_0, z_0) is the sphere center, and $p(x, y, z)$ represents the measured points.

Using this method, the cavity material removal volume was calculated as $2.3 \times 10^7 \mu m^3$, corresponding to an MRR of $1.42 \times 10^4 \mu m^3 / s$. The surface roughness from 3D topography measurements was $S_a = 3.2 \mu m$. These results, combined with low form error (RMS ≈ 3.4 µm; NRMS ≈ 2.07%), confirm the high-accuracy performance of the wire-renewal EDM process.

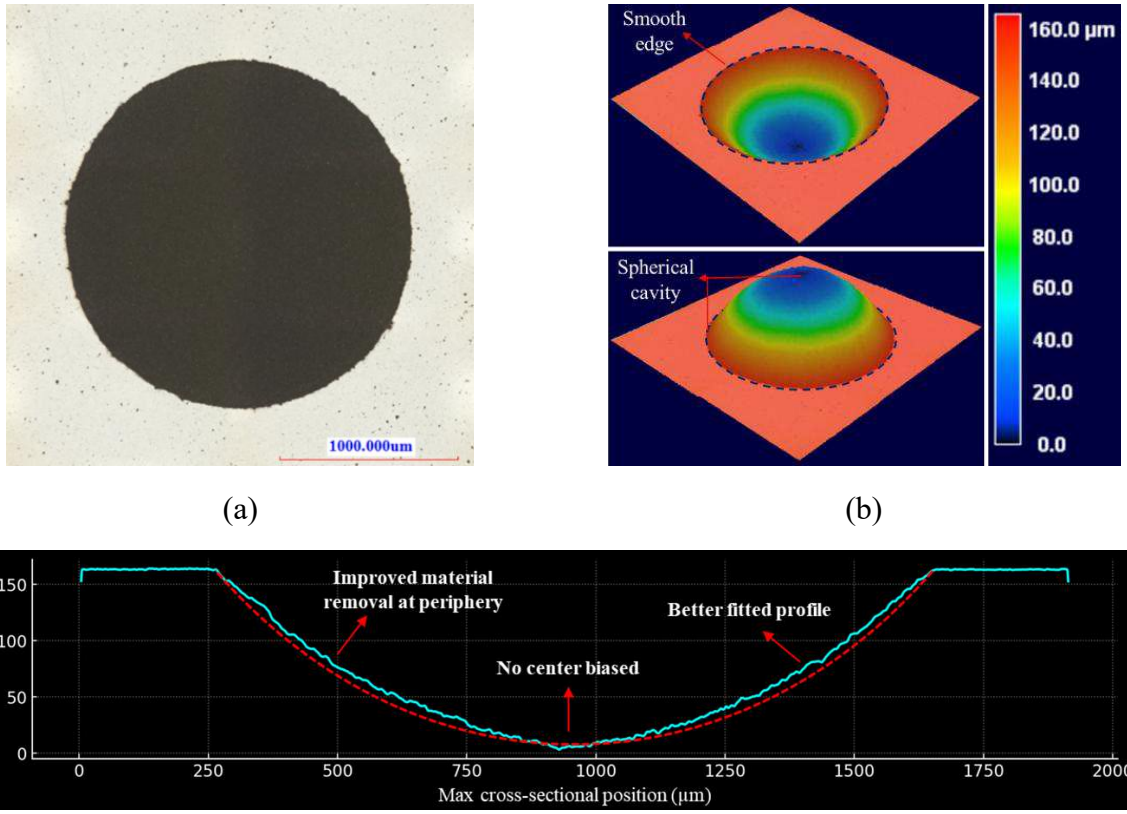
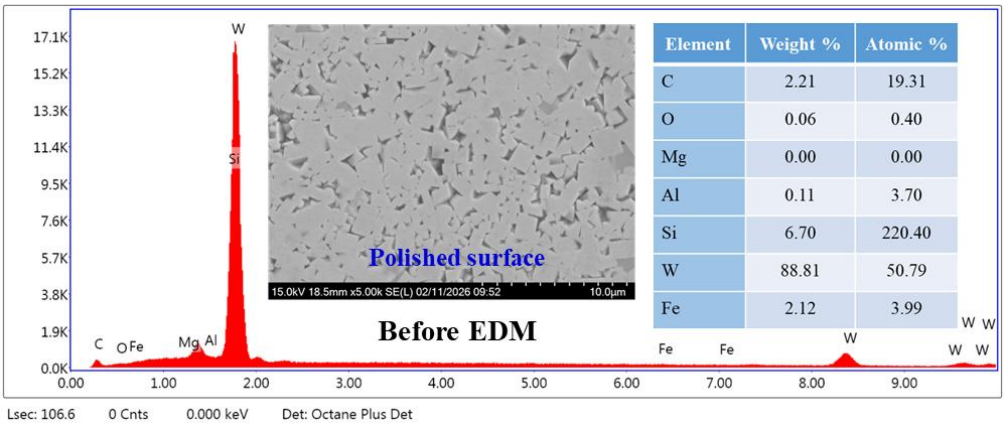


Figure. 16 EDM surface after parametric optimization: (a) optical top view of machined surface; (b) 3D topography of spherical profile; (c) Cross-sectional profile demonstrating improved fitting.

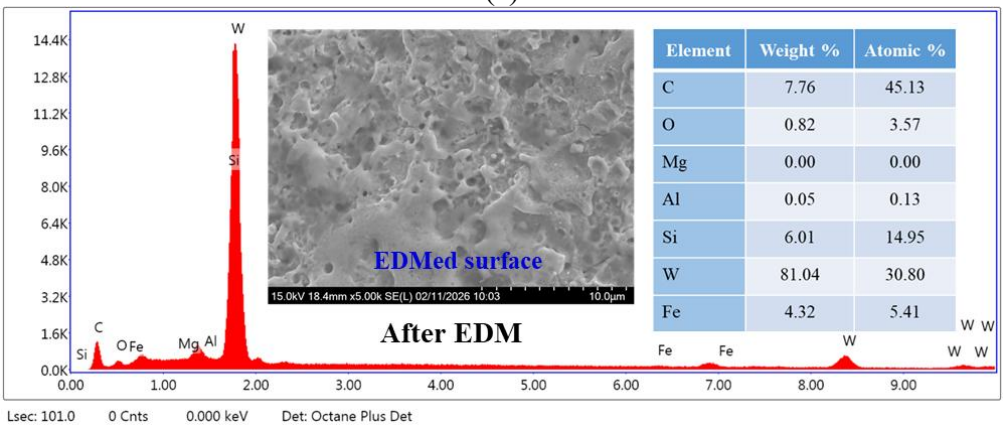
As shown in Fig. 17, the EDS analysis of WC before and after EDM. The elemental analysis of the pre-EDM surface (Fig. 17a) presents a high concentration of tungsten (88.81%) and carbon (2.21%), consistent with the WC phase and its carbide binder. Additionally, small amounts of oxygen (0.06%) and iron (2.12%) were detected, which may be linked to surface oxidation or contamination from the machining environment. After the EDM process (Fig. 17b), significant changes were observed. The tungsten content (81.04%) decreased slightly, indicating selective erosion of the binder phase, while the carbon content (7.76%) increased, reflecting the thermal decomposition of WC and the formation of graphite in the resolidified layer under high-temperature discharge conditions. The oxygen content increased to 0.82%, suggesting the formation of surface oxidation during the EDM process. The iron (4.32%) content increased, which could be attributed to contamination from the EDM electrode or dielectric fluid, while

silicon content remained relatively unchanged at 6.01%, indicating the presence of impurities or additives in the dielectric medium.



Element	Weight %	Atomic %
C	2.21	19.31
O	0.06	0.40
Mg	0.00	0.00
Al	0.11	3.70
Si	6.70	220.40
W	88.81	50.79
Fe	2.12	3.99

(a)



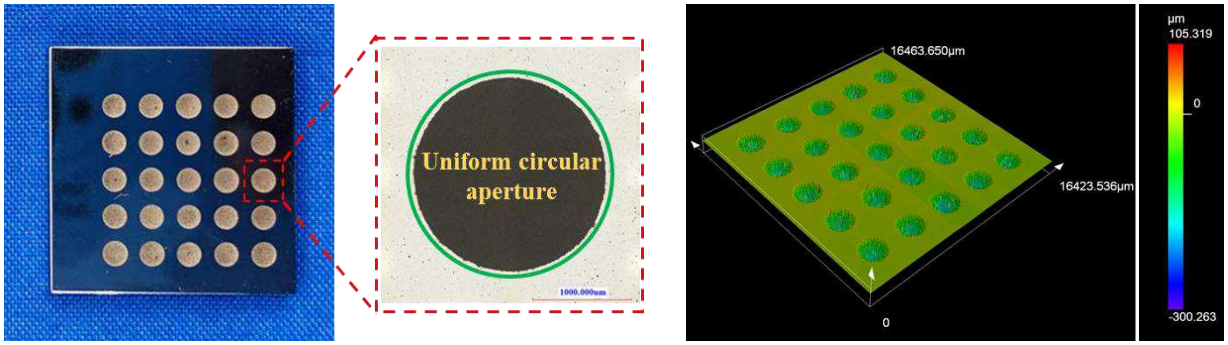
Element	Weight %	Atomic %
C	7.76	45.13
O	0.82	3.57
Mg	0.00	0.00
Al	0.05	0.13
Si	6.01	14.95
W	81.04	30.80
Fe	4.32	5.41

(b)

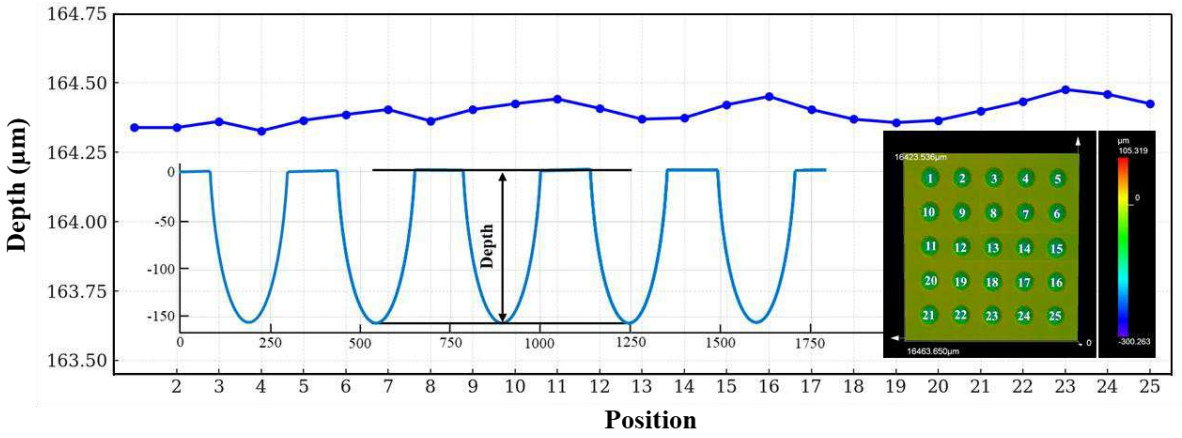
Figure. 17 Surface composition analysis of WC workpiece: (a) before EDM; (b) after EDM.

4.3 Fabrication of MLA Mold by Wire-shift Stepping

The fabrication of the MLA mold was accomplished through a repeated cycle of electrode approach, dwell, wire renewal, and stage indexing at each programmed grid coordinate. At each site, the electrode advanced to the prescribed working gap and dwelled to achieve the target depth, while the wire segment was incrementally advanced to expose an unworn portion, ensuring consistent discharge conditions.



(a) (b)



(c)

Figure. 18 Fabrication of the (5×5) MLA mold using wire-shift stepping: (a) optical photograph of uniform MLA mold; (b) 3D surface topography of the mold; (c) depth for each lenslet.

As shown in Fig. 18(a), the optical image confirms the regularity and uniformity of the lenslet array. The resulting MLA (5×5) mold showed uniform circular apertures, with no peripheral lips observed in the top-view images. As shown in Fig. 18(b), 3D surface topography confirmed array-level coplanarity and regular spacing, indicating stable discharge behavior and effective wire renewal throughout the fabrication process. The extracted maximum depth of a single microlens at different positions is shown in Fig. 18(c). The depths of microlens units from 1 to 25 are about 164 ± 0.3 μm, which indicates high uniformity and consistent fabrication across the array.

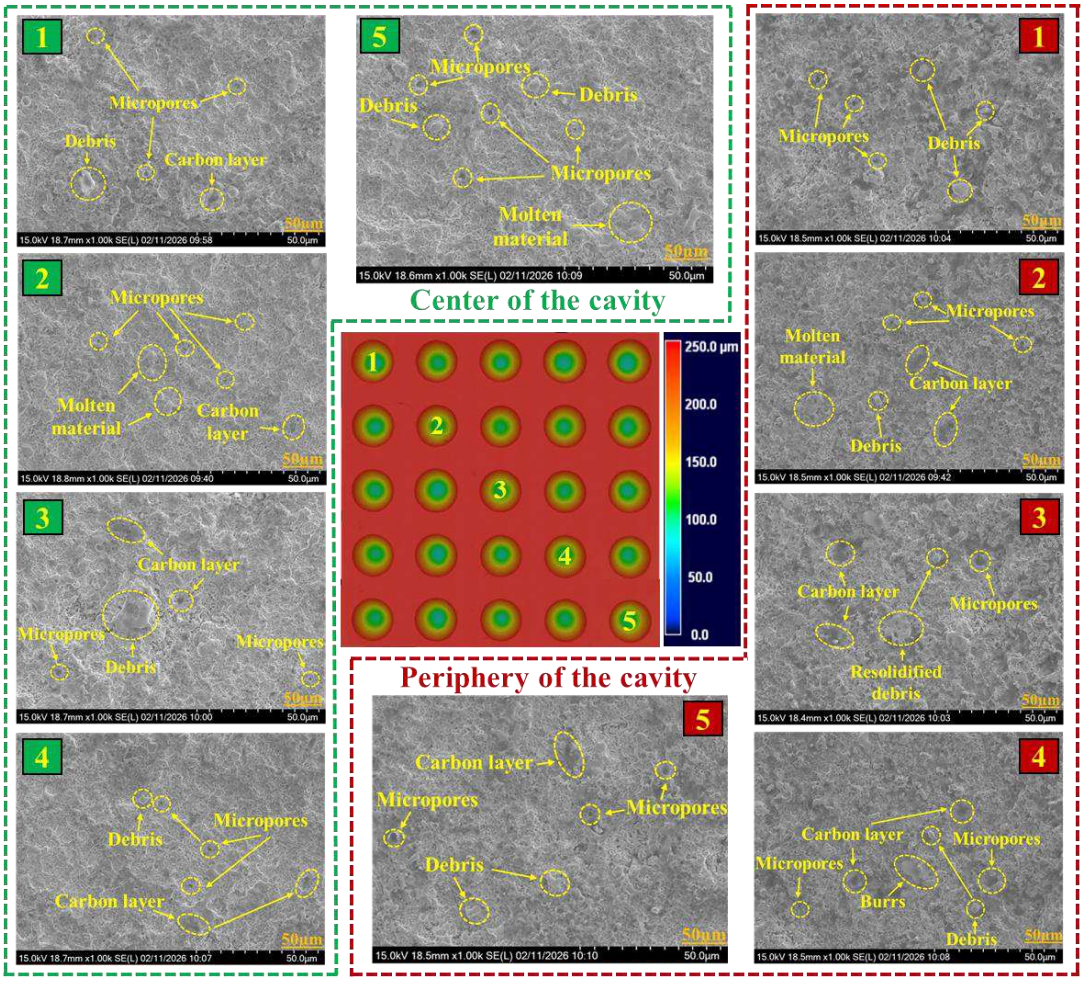


Figure. 19 SEM characterization in two different positions of the fabricated MLA mold.

The SEM analysis (Fig. 19) provides detailed insights into the surface morphology of the fabricated MLA mold under optimized EDM parameters. At the central regions of different cavities, the surface shows a high density of uniform micropores with smooth resolidified rims. This morphology indicates consistent material removal and controlled thermal cycling, reflecting the effectiveness of the wire-renewal EDM milling process in maintaining a stable discharge during dwell. The crater sizes are highly uniform across all cavities, suggesting reproducible energy deposition at the focal point of each microlens. In the peripheral regions, it shows slightly larger but equally regular micropores, with no observable burr formation, edge ridges, or recast irregularities.

5. Conclusion

In this study, a novel wire-renewal EDM milling electrode has been proposed to address the limitations of conventional EDM in fabricating MLA molds on tungsten WC. The electrode design, incorporating a precision-contoured groove for continuous wire renewal, enabled a stable annular discharge, uniform material removal, and consistent replication of the spherical-cap cavity geometry. The process mitigated the challenges associated with conventional EDM, such as

cumulative electrode wear and form degradation. The key findings and implications are summarized as follows:

1. The wire-renewal EDM milling electrode design, featuring a spherical head with a precision-contoured groove supporting a continuously tensioned copper wire, enables in-situ wire renewal. This ensures the stabilization of discharge geometry, minimizes electrode wear, and reduces the need for frequent electrode replacement, thus enhancing the efficiency and accuracy of MLA mold fabrication.

2. A comprehensive analysis of key process parameters, including spindle rotation speed, pulse timing, servo voltage, and peak current, demonstrated their influence on cavity geometry. In particular, rotation and pulse timing were found to be critical in mitigating center-biased material removal, ensuring symmetric and uniform microlens cavities, while voltage and current acted as secondary tuning factors. Under the optimized conditions, the fabricated microlens cavities exhibited high fidelity, with a sag depth of ~160 μm, low form error (RMS ≈ 3.4 μm; NRMS ≈ 2.07%), and consistent surface roughness of 3.2 μm, confirming the effectiveness of the wire-renewal EDM milling method for high-precision fabrication.

3. The proposed method successfully fabricated a (5×5) MLA mold, demonstrating excellent uniformity, consistent depth, and **c**oplanarity across the array. This highlights the potential of the wire-renewal EDM milling strategy, providing a robust and reproducible method for large-scale production of high-precision structured molds on hard materials.

The findings highlight the potential of the wire-renewal EDM milling electrode to revolutionize EDM-based micro-optical manufacturing, enabling cost-effective fabrication of microlens array molds. Future work will focus on refining surface quality and investigating advanced post-processing techniques to further enhance shape accuracy and finish.

CRediT authorship contribution statement

Md Nasir Uddin: Conceptualization, Methodology, Formal analysis, Investigation, Writing - review & editing. Fubin Ma: Investigation, Methodology.Tianfeng Zhou: Conceptualization, Methodology, Funding acquisition, Writing - review & editing, Supervision. Liheng Gao: Methodology, Formal analysis. Gang Wang: Formal analysis. Weijia Guo: Conceptualization, Investigation, Writing – review & editing.

Declaration of Competing Interest

The authors declare that they have no known competing financial interests or personal relationships that could have appeared to influence the work reported in this paper.

Acknowledgement

This work was financially supported by the National Natural Science Foundation of China (52405451).

References

[1] X. Wang, C. Liu, L. Qiao, J. Zhou, Y. Bai, J. Sun, Imaging with high resolution and wide field of view based on an ultrathin microlens array, Phys. Rev. Applied 21 (2024) 034035. https://doi.org/10.1103/PhysRevApplied.21.034035.

[2] V.T. Vu, H. Yi, Y. Park, H. Lee, Image Quality Analysis and Testing Process for Microlens Array-Based Optical Devices with High-Resolution Image Reconstruction, Int. J. Precis. Eng. Manuf. 26 (2025) 1215–1225. https://doi.org/10.1007/s12541-024-01179-1.

[3] J. Lim, P. Gruner, M. Konrad, J.-C. Baret, Micro-optical lens array for fluorescence detection in droplet-based microfluidics, Lab Chip 13 (2013) 1472. https://doi.org/10.1039/c3lc41329b.

[4] S. Royo, M. Ballesta-Garcia, An Overview of Lidar Imaging Systems for Autonomous Vehicles, Applied Sciences 9 (2019) 4093. https://doi.org/10.3390/app9194093.

[5] R.J. Lin, V.-C. Su, S. Wang, M.K. Chen, T.L. Chung, Y.H. Chen, H.Y. Kuo, J.-W. Chen, J. Chen, Y.-T. Huang, J.-H. Wang, C.H. Chu, P.C. Wu, T. Li, Z. Wang, S. Zhu, D.P. Tsai, Achromatic metalens array for full-colour light-field imaging, Nat. Nanotechnol. 14 (2019) 227–231. https://doi.org/10.1038/s41565-018-0347-0.

[6] M. Schambach, F.P. León, Microlens Array Grid Estimation, Light Field Decoding, and Calibration, IEEE Trans. Comput. Imaging 6 (2020) 591–603. https://doi.org/10.1109/TCI.2020.2964257.

[7] R. Zhao, X. Hua, W. Baek, Z. Wang, S. Jia, L. Gao, A review of light-field imaging in biomedical sciences, Med-X 3 (2025) 25. https://doi.org/10.1007/s44258-025-00070-6.

[8] K.-C. Kwon, K.H. Kwon, M.-U. Erdenebat, T. Amgalan, H.-Y. Wu, A. Khuderchuluun, K.H. Yoo, N. Kim, High-fidelity 3D visualization system for light field microscopy based on zonal-multiplexed holographic optical element-microlens array, Optics and Lasers in Engineering 196 (2026) 109432. https://doi.org/10.1016/j.optlaseng.2025.109432.

[9] P. Fan, F. Li, L. Li, Z. Hu, Measurement of virtual image distance in augmented reality or virtual reality devices based on microlens array wavefront division, in: C. Ping (Ed.), Tenth Symposium on Novel Optoelectronic Detection Technology and Applications, SPIE, Taiyuan, China, 2025: p. 92. https://doi.org/10.1117/12.3056074.

[10] N. Incardona, S. Coppola, V. Vespini, S. Grilli, J. Behal, L. Miccio, V. Bianco, M. Martinez-Corral, P. Ferraro, Self-assembling of PDMS microlens arrays through pyro-EHD for real-time 3D microscopy, Optics and Lasers in Engineering 178 (2024) 108239. https://doi.org/10.1016/j.optlaseng.2024.108239.

[11] C. Kim, M. Lee, Microlens array-based plenoptic microscopy for high-precision 3D imaging, in: X. Shen, B. Javidi, A. Anand (Eds.), Three-Dimensional Imaging, Visualization, and Display 2025, SPIE, Orlando, United States, 2025: p. 52. https://doi.org/10.1117/12.3053914.

[12] F. Sun, Y. Huang, S. Cheng, S. Huang, X. Wang, J. Zhu, W. Lu, Y. Ding, T. Wu, J. Ma, Y. Liu, J. Shen, Precision glass molding with high-temperature metallic glass as inserts, Sci. China Technol. Sci. 68 (2025) 1920204. https://doi.org/10.1007/s11431-025-2997-0.

[13] K. Li, C. Wang, F. Gong, The Filling Ratio and Surface Roughness Evolution of Glass Array Lens in Precision Glass Molding, Nanomanuf Metrol 8 (2025) 2. https://doi.org/10.1007/s41871-025-00250-3.

[14] F. Ma, T. Zhou, M.N. Uddin, Y. Cui, J. Zeng, X. Wang, W. Guo, Manufacturing high-consistency microlens arrays on tungsten carbide via electrical discharge machining using micro copper ball–assembled array electrode, Int J Adv Manuf Technol 135 (2024) 3405–3419. https://doi.org/10.1007/s00170-024-14714-1.

[15] K. Egashira, S. Hosono, S. Takemoto, Y. Masao, Fabrication and cutting performance of cemented tungsten carbide micro-cutting tools, Precision Engineering 35 (2011) 547–553. https://doi.org/10.1016/j.precisioneng.2011.06.002.
[16] S. Wang, H. Liu, B. Wu, W. Zong, Theoretical and experimental insights into microstructure effects on WC machinability, Journal of Manufacturing Processes 153 (2025) 378–389. https://doi.org/10.1016/j.jmapro.2025.09.013.
[17] S. Deng, Y. Xia, M. Wu, D. Lei, Q. Zhang, Nanosecond Laser Ablation Assisted Precision Grinding of WC/Co Cemented Tungsten Carbide, Int. J. Precis. Eng. Manuf. 26 (2025) 283–294. https://doi.org/10.1007/s12541-024-01103-7.
[18] M. Zhang, Z. Pang, Y. Jia, C. Shan, Understanding the machining characteristic of plain weave ceramic matrix composite in ultrasonic-assisted grinding, Ceramics International 48 (2022) 5557–5573. https://doi.org/10.1016/j.ceramint.2021.11.100.
[19] M. Choubey, K. Maity, S. Bansal, P. Kumar, Machinability of Tungsten Carbide Through Electrical Discharge Machining: State of Art and Future Perspectives, Proc. Natl. Acad. Sci., India, Sect. A Phys. Sci. (2025). https://doi.org/10.1007/s40010-025-00964-5.
[20] André Filipe Varandas Pedroso, R. Lucas, L. Teixeira, R.D.S.G. Campilho, A.G. Pinto, R. Costa, R.D.C.M. Sales-Contini, Electrical Discharge Machining of Composites: A Critical Review of Challenges and Innovations, JMEM (2025) 5. https://doi.org/10.53941/jmem.2025.100005.
[21] T. Zhou, C. Zhou, Z. Liang, X. Wang, Machining mechanism in tilt electrical discharge milling for lens mold, Int J Adv Manuf Technol 95 (2018) 2747–2755. https://doi.org/10.1007/s00170-017-1408-5.
[22] K. Jangra, S. Grover, A. Aggarwal, Optimization of multi machining characteristics in WEDM of WC-5.3%Co composite using integrated approach of Taguchi, GRA and entropy method, Front. Mech. Eng. 7 (2012) 288–299. https://doi.org/10.1007/s11465-012-0333-4.
[23] G. Talla, S. Gangopadhyay, N.B. Kona, Experimental investigation and optimization during the fabrication of arrayed structures using reverse EDM, Materials and Manufacturing Processes 32 (2017) 958–969. https://doi.org/10.1080/10426914.2016.1221085.
[24] Z. Zhang, H. Yu, Y. Zhang, K. Yang, W. Li, Z. Chen, G. Zhang, Analysis and optimization of process energy consumption and environmental impact in electrical discharge machining of titanium superalloys, Journal of Cleaner Production 198 (2018) 833–846. https://doi.org/10.1016/j.jclepro.2018.07.053.
[25] W. Wu, X.-Y. Wu, J.-G. Lei, B. Xu, K. Jiang, Z.-Z. Wu, H.-M. Yin, W. Li, Fabrication of deep-narrow microgrooves by micro-EDM using rotary dentate disc foil electrodes in emulsion, J. Micromech. Microeng. 29 (2019) 035014. https://doi.org/10.1088/1361-6439/ab0001.
[26] H. Dong, Y. Liu, M. Li, T. Liu, Y. Zhou, D. Li, Y. Shen, High-speed compound sinking machining of Inconel 718 using water in oil nanoemulsion, Journal of Materials Processing Technology 274 (2019) 116271. https://doi.org/10.1016/j.jmatprotec.2019.116271.
[27] M.P. Garg, A. Kumar, C.K. Sahu, Mathematical modeling and analysis of WEDM machining parameters of nickel-based super alloy using response surface methodology, Sādhanā 42 (2017) 981–1005. https://doi.org/10.1007/s12046-017-0647-3.
[28] K. Jiang, X. Wu, J. Lei, Z. Hu, G. Gao, Y. Tang, D. Diao, Investigation on the geometric evolution of microstructures in EDM with a composite laminated electrode, Journal of Cleaner Production 298 (2021) 126765. https://doi.org/10.1016/j.jclepro.2021.126765.

[29] S.-H. Chou, A.-C. Wang, Investigating and removing the re-sticky debris on tungsten carbide in electrical discharge machining, Int J Adv Manuf Technol 71 (2014) 1151–1158. https://doi.org/10.1007/s00170-013-5556-y.
[30] J. Pei, X. Zhuang, L. Zhang, Y. Zhu, Y. Liu, An improved fix-length compensation method for electrical discharge milling using tubular tools, International Journal of Machine Tools and Manufacture 124 (2018) 22–32. https://doi.org/10.1016/j.ijmachtools.2017.09.005.
[31] H. Takino, T. Hosaka, Shaping of steel mold surface of lens array by electrical discharge machining with single rod electrode, Appl. Opt. 53 (2014) 8002. https://doi.org/10.1364/AO.53.008002.
[32] B. Xu, X. Wu, J. Lei, R. Cheng, S. Ruan, Z. Wang, Laminated fabrication of 3D micro-electrode based on WEDM and thermal diffusion welding, Journal of Materials Processing Technology 221 (2015) 56–65. https://doi.org/10.1016/j.jmatprotec.2015.02.005.
[33] L. Gu, L. Li, W. Zhao, K.P. Rajurkar, Electrical discharge machining of Ti6Al4V with a bundled electrode, International Journal of Machine Tools and Manufacture 53 (2012) 100–106. https://doi.org/10.1016/j.ijmachtools.2011.10.002.
[34] K.Y. Song, D.K. Chung, M.S. Park, C.N. Chu, Electrical discharge machining using a strip electrode, Precision Engineering 37 (2013) 738–745. https://doi.org/10.1016/j.precisioneng.2013.02.006.
[35] K. Li, C. Wang, F. Gong, C.F. Cheung, Facile and flexible fabrication of structured array surfaces on binderless tungsten carbide by using electrical discharge machining with a novel self-assembly ball electrode, (n.d.).

Supplementary Files

This is a list of supplementary files associated with this preprint. Click to download.

- Graphicalabstract.png